AGU PUBLICATIONS

JGR

Journal of Geophysical Research: Oceans

RESEARCH ARTICLE

10.1002/2017JC013400

Reconstruction of the 3-D Dynamics From Surface Variables in a High-Resolution Simulation of North Atlantic

S. Fresnay[1], A. L. Ponte[2], S. Le Gentil[2], and J. Le Sommer[3]

[1]OceanDataLab, Brest, France, [2]Univ. Brest, CNRS, IRD, Ifremer, Laboratoire d'Océanographie Physique et Spatiale, IUEM, Brest, France, [3]Univ. Grenoble-Alpes, CNRS, IRD, IGE, Grenoble, France

Key Points:
- In the Gulf Stream area, sea level is a better predictor of pressure and potential vorticity compared to surface temperature and salinity
- Estimating pressure at depth from an inversion of potential vorticity or a direct linear regression from sea level have comparable skills
- The depth of skillful reconstructions decreases from more than 1,000 m at scales larger than 200 km down to 200 m at 100 km wavelengths

Supporting Information:
- Supporting Information S1
- Movie S1

Correspondence to:
S. Fresnay,
simon.fresnay@oceandatalab.com

Citation:
Fresnay, S., Ponte, A. L., Le Gentil, S., & Le Sommer, J. (2018). Reconstruction of the 3-D dynamics from surface variables in a high-resolution simulation of North Atlantic. *Journal of Geophysical Research: Oceans*, *123*, 1612–1630. https://doi.org/10.1002/2017JC013400.

Received 30 AUG 2017
Accepted 30 JAN 2018
Accepted article online 5 FEB 2018
Published online 1 MAR 2018

Abstract Several methods that reconstruct the three-dimensional ocean dynamics from sea level are presented and evaluated in the Gulf Stream region with a 1/60° realistic numerical simulation. The use of sea level is motivated by its better correlation with interior pressure or quasi-geostrophic potential vorticity (PV) compared to sea surface temperature and sea surface salinity, and, by its observability via satellite altimetry. The simplest method of reconstruction relies on a linear estimation of pressure at depth from sea level. Another method consists in linearly estimating PV from sea level first and then performing a PV inversion. The last method considered, labeled SQG for surface quasi-geostrophy, relies on a PV inversion but assumes no PV anomalies. The first two methods show comparable skill at levels above −800 m. They moderately outperform SQG which emphasizes the difficulty of estimating interior PV from surface variables. Over the 250–1,000 m depth range, the three methods skillfully reconstruct pressure at wavelengths between 500 and 200 km whereas they exhibit a rapid loss of skill between 200 and 100 km wavelengths. Applicability to a real case scenario and leads for improvements are discussed.

1. Introduction

A fundamental challenge for the estimation of the time varying ocean circulation lies in the scarcity of available observations (Wunsch, 2015). Satellite remote sensing of sea surface height (SSH) may be linked to the circulation at the surface via geostrophy but suffers in general from a moderate spatial and temporal resolution with respect to mesoscales and submesoscales. Wide-swath altimetry (SWOT, launch date 2021) should improve the spatial coverage of SSH observations (Fu et al., 2012). Satellite observations of sea surface temperature and salinity may also provide useful information about the ocean circulation (Reul et al., 2014; Rio et al., 2016) that is not unrelated to SSH (Hausmann & Czaja, 2012; Jones et al., 1998). Leveraging useful information from these tracers is however complicated by poorly constrained surface mixed layer dynamics and surface fluxes and/or data availability and resolution (Chelton & Wentz, 2005; Rio et al., 2016). The global Argo network provides hydrographic profiles that contain the signature of the time varying ocean circulation, but its temporal coverage is limited by the time interval between profiles (about 10 days) and float separation (about 300 km; Le Traon, 2013), which is again coarse compared to mesoscale and submesoscale spatiotemporal scales of evolution.

Statistical and/or dynamical models are thus necessary in order to fill in data gaps and combine the information brought by observations of different nature. Trade-offs must in general be dealt with between dynamical model complexity, required computational effort, a priori statistical information and assumptions, and, data quantity and quality. Data assimilation with dynamical models based on primitive equations is one solution, for example, that, unfortunately, remains computationally expensive and resolves mesoscales in regional configurations only (Edwards et al., 2015). Methods that rely, on the other hand, exclusively on statistical models correlate collocated observations of remotely sensed SSH and, with a smaller impact, SST with in situ Argo temperature and salinity data (Guinehut et al., 2006, 2012). These correlations may then be leveraged to infer from SSH and SST interior dynamic heights and currents assuming geostrophy (Mulet et al., 2012). The validity of such approach is then given by these same correlations which vary geographically. Its performance as a function of spatial scales remains unknown. Various flavors of such methods have been used in order to mitigate the impact of the noise due to the time varying ocean fluctuations on estimations of time mean variables (Rio & Hernandez, 2004; Willis & Fu, 2008). Current meter records have occasionally been analyzed in order to describe the characteristic vertical structure of ocean fluctuations and

improve means of interpreting and extrapolating satellite observations (of SSH in particular). Wunsch (1997) forced a fit onto vertical normal modes which are a natural dynamical basis of projection for a flat ocean and a spatially uniform stratification. They found that, on average, the barotropic and first baroclinic modes dominate the depth-integrated kinetic energy. Because of its surface intensification near the surface however, the first baroclinic mode dominates the surface kinetic energy and thus SSH expectedly. This was argued to explain the poor interpretative value of barotropic models in explaining altimetric observations of SSH. This is consistent with Stammer (1997) conclusion based on the tight relationship between altimetric decorrelation length scales and Rossby radii of deformation and with Smith and Vallis (2001) findings that there is a piling of energy at the lowest baroclinic mode because of the oceanic pycnocline in idealized numerical simulations of ocean turbulence. Interestingly, Wunsch (1997) found temporal and geographical variations of their results and a certain degree of modal coupling. Such coupling led Sanchez de La Lama et al. (2016) to compute empirical orthogonal modes (EOF) of current meter records. The first EOF at most locations appeared to explain more than half of the current meter variance (their Figure 4). The associated vertical structures were found to be decreasing functions of depth and close to the normal modes derived when assuming no normal flow at depth.

Lapeyre and Klein (2006) initiated a different branch of studies whose roots lie in the expected quasi-geostrophic (QG) behavior of mesoscale motions. The state of a QG system is entirely given by QG potential vorticity (PV) and top/bottom densities (which Bretherton (1966) understood as sheets of PV). One appeal of this framework is that it provides means to link SSH, which is pressure at the sea surface, and, SST, which is related to surface density. One may actually decompose the flow into a surface QG (SQG) contribution associated with surface density anomalies but no interior PV, and, an interior contribution associated with zero surface density anomalies but nonzero interior PV. The SQG contribution is solely given by the surface density anomaly and the stratification, and, the associated stream function is a decreasing function of depth consistently with current meter records. This contribution may be estimated from satellite observations of SST and be useful in order to estimate the circulation at the surface under particular conditions (deep mixed layers for example; Isern-Fontanet et al., 2006, 2008). Lapeyre (2017) presents an extensive review about SQG. In the general case however, the interior contribution is significant such that PV needs to be estimated from observations. Lapeyre and Klein (2006), LaCasce and Mahadevan (2006), and Lapeyre (2009) argue that a linear relationship between SST or surface density and PV may be leveraged in order to so. Ponte and Klein (2013) assume a correlation between near-surface PV and PV deeper within the water column. Wang et al. (2013) circumvents the estimation of PV by reducing the vertical representation of the flow to a SQG mode plus a barotropic mode plus a first baroclinic mode, and, by constraining these modes with a knowledge of sea level, surface density, and, an assumption of no flow at depth. The purpose of the present work is to investigate whether reconstructions of PV from observable surface variables do improve our ability to estimate the ocean circulation from these variables.

We focus on a particular region that contains the propagation of the Gulf Stream (GS) starting at its separation with the shelf near Cape Hatteras up to 1,500 km eastward. The presence of a strong frontal feature such as the GS is thought to be favorable to estimations of interior PV from observations of surface variables (Lapeyre & Klein, 2006). The GS variability and dynamics, along with the generation of cold-core and warm-core rings, have been extensively studied from both observations (Meinen & Luther, 2016; Olson, 1991; Rossby et al., 2010; The Ring Group, 1981), numerical models (Kang & Curchitser, 2013, 2015) and theory (Sutyrin, 2015). Several studies focused on the deep cyclogenesis events occurring on the main GS path and noted that it is synchronous with upper level meander steepenings (Savidge & Bane, 1999; Shay et al., 1995; Watts et al., 1995). Meinen and Luther (2016) found some vertical coherence of velocity inferred from pressure-equipped inverted echo sounders at high frequencies (periods lower than 50 days), but the vertical extent of the coherence was limited such that the authors concluded that observable surface proxies might not provide useful information about the flow at and below the thermocline. Savidge (2016) argued that this lack of coherence may be due to the spatial averaging employed in Meinen and Luther (2016)'s analysis prior to computations of vertical coherence. On the basis of a dense time sampling of current vertical profiles, Lindstrom et al. (1997) suggested that the mean meander of the GS between −65°W and −70°W have actually a phase tilt with depth. The relative smallness of the phase tilt (between one sixth and one sixteenth of an upper level wavelength with a decreasing tendency at the time of maximum deep cyclone strength) supports the idea that the result of Meinen and Luther (2016) might not be a general property of

the GS (Savidge & Bane, 1999; Watts et al., 1995). The vertical structure of PV fluctuations received less attention in observations but Lapeyre (2009) found some correlation between near-surface buoyancy and PV within the first 500 m in the GS region.

The present article is structured as follows. In the first two parts, we present the simulation and the background state in the Gulf Stream area (section 2) and describe, for one date, the pattern of the QG variables (pressure and PV; section 3). We perform afterward a correlation analysis between QG variables and surface variables on the full 2 year period which highlights the predicting skill of SSH (section 4). From the previous result, several reconstructions of the QG variables are investigated on one date, with or without a PV constraint, and compared (section 5). Additional discussion is given in section 6, emphasizing the differences between the two variables (pressure and PV) and providing more information on the distribution of the reconstruction skill (via spectral analysis) and its temporal variation (three other dates have been studied).

2. Data, Region, and Method

2.1. The Simulation

The numerical simulation NATL60 is a primitive-equation high-resolution simulation of the North Atlantic, based on the NEMO core (Madec & The NEMO Team, 2008), carried out by MEOM/IEG (Multiscale Ocean Modelling/Institut des Géosciences de l'Environnement, Grenoble). The horizontal grid of NATL60 is a refinement of the 1/12° ORCA global tripolar grid (Madec & Imbard, 1996) on the North Atlantic Domain to 1/60° resolution, i.e., the mesh size varies from 1,600 m on the southern boundary to 900 m on the northern boundary and is about 1.3 km in the Gulf Stream region. The vertical grid has 300 levels and the vertical spacing decreases from 50 m at −6,000 to 1 m at the surface. The bathymetry of the model is based on GEBCO008 and GTOPO30 (https://lta.cr.usgs.gov/GTOPO30) data sets.

Advection scheme is FCT (second order centered scheme with corrected flux) for tracers and energy-enstrophy conserving scheme for momentum (Barnier et al., 2006; Le Sommer et al., 2009). The vector form momentum advection scheme is modified in order to remove a spurious numerical instability (Ducousso et al, 2017). Lateral turbulent parameterizations include an isopycnal Laplacian diffusion of tracers with a coefficient that decreases linearly as a function of grid size from 20 m^2/s at the southern boundary to 9 m^2/s at the northern boundary. This is combined with biharmonic diffusion of momentum with a coefficient A_v that decreases from the southern boundary, where $A_v = 3.3\times10^7$ m^4/s, toward the northern boundary. Vertical turbulence parameterizations are achieved with a turbulent kinetic energy (TKE) closure, which is based on a prognostic equation for TKE and a closure assumption for the turbulent length scales (Gaspar et al., 1990), plus an enhanced vertical mixing of tracers and momentum in case of static instability (Madec & The NEMO Team, 2008). Quadratic bottom friction and free-slip lateral boundary conditions are used.

Initial and lateral open boundary conditions are provided by monthly averages of the GLORYS2 reanalysis (Ferry et al., 2012). The simulation is performed with a free surface but constant volume is imposed. It is forced realistically at the surface by radiative/heat/water fluxes, atmospheric pressure and windstress provided by the DRAKKAR Forcing Set version 5.2 (Dussin et al., 2014), derived from the atmospheric reanalysis ERA-Interim. Penetrative solar radiation is based on clear water only with a penetration length of 17 m. Continental runoffs are calculated from monthly climatologies (Dai & Trenberth, 2002).

NATL60 spin-up period extends from January 2004 to November 2006. The present analysis is based on 2007 and 2008 outputs.

2.2. Pressure, Stream Function, and Potential Vorticity

Pressure normalized by the reference density $\rho_0 = 1,000$ kg/m^3 writes

$$p = g\left(\int_{-z}^{0} \rho dz + \mathrm{SSH}\right) \tag{1}$$

using the normalized density $\rho(x,y,z,t) = \rho_0^{-1}[\tilde{\rho}(x,y,z,t) - \bar{\rho}(z)]$, where $\tilde{\rho}$ is the in situ density, and, where the reference density profile $\bar{\rho}(z)$ has been computed in the present study as the spatial (see section 2.3) and temporal (2007–2008) average of temperature and salinity over the 2 years of the simulation. The geostrophic stream function is

$$\psi = p/f_0 \tag{2}$$

where f_0 is the domain-averaged Coriolis parameter.

QG potential vorticity writes

$$q = \nabla^2\psi + f - f_0 + \partial_z \frac{f_0^2}{N^2}\partial_z\psi \tag{3}$$

where ∇^2 stands for the horizontal laplacian, f is the local Coriolis parameter, and $N^2(z)$ is the squared Brunt-Vaisala frequency associated to the background stratification $\bar{\rho}(z)$. We have computed PV from density and SSH of the model using (1) and (2), i.e.,

$$q = \nabla^2 p/f_0 + f - f_0 - g f_0 \partial_z \frac{\rho}{N^2} \tag{4}$$

Note that the values of q do depend on the reference profile chosen, which is notably dependent on the domain chosen for spatial averaging.

For the sake of simplicity, we will use "potential vorticity" or "PV" in the forthcoming development for q defined by (3) or (4).

2.3. The Gulf Stream Domain

Data used in this study focuses on a region which extends from −75°W to −58°W and from 31°N to 41°N, thereby covering meanders of the Gulf Stream (GS) immediately east of the Cape Hatteras and a part of the Sargasso Sea (Figure 1a). More than 80% (resp. 75%) of the horizontal domain area is deeper than 3,000 m (resp. 4,000 m), which allows one to interpret domain horizontal averages down to this depth with a good confidence. Levels deeper than 5,000 m are more weakly represented (less than 35% of the horizontal domain area).

The location of maximum of meridional gradient of time-averaged SSH represents the Gulf Stream (GS) mean path. It exhibits downstream of Cape Hatteras a ridge with anticyclonic curvature at about −71°W followed by a crest of cyclonic curvature at about −69°W (Figure 1a). Other meanders may be seen east of −66°W. Horizontal patterns of SSH rms emphasize that most of the ocean variability (GS meanders, eddies) is tightly related with the GS mean path, as expected (Ducet et al., 2000; Kang & Curchitser, 2013).

A reference profile of stratification $N^2(z)$ is computed from a temporal (2007–2008) and spatial average of temperature and salinity (Figure 1b). The profile exhibits a local maximum about the −800 m level, a local minimum about the −400 m level and a maximum within the first hundred meters. It is typical of waters of the western part of the North Atlantic subtropical gyre which have a permanent signature of the high

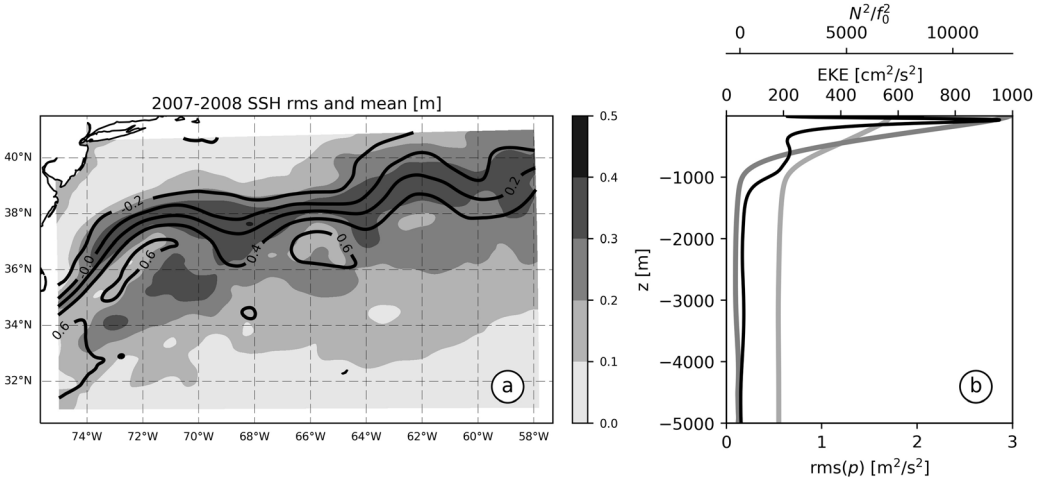

Figure 1. (a) SSH time rms (shaded, unit: m) and mean (black contour, interval: 0.2 m) from the NATL60 simulation in the Gulf Stream domain; (b) horizontally averaged vertical profile of N^2 (black), time-averaged EKE (dark gray), and pressure time rms (light gray). See text for the definition of N^2. Statistics were computed over the 2007–2008 period.

surface stratification (the maximum occurs in summer) and of a deep pycnocline (Feucher et al., 2016). This results from the larger weight of subtropical waters (southward of the line 0 of the mean SSH in Figure 1a) in horizontal averages within the present domain.

Vertical profiles of eddy kinetic energy (EKE) and pressure rms (Figure 1b) are surface intensified with lowest and approximately constant values below the −1,000 m level (less than 100 cm^2/s^2 for EKE and 0.7 m^2/s^2 for pressure rms) and maximum values at the surface (1,000 cm^2/s^2 for EKE and 3 m^2/s^2 for pressure rms). Maximum of EKE occurs over the GS with values of about 4,000 cm^2/s^2 at −69°W (not shown). These numbers are comparable to other analyses (Ducet et al., 2000; Kang & Curchitser, 2013). The similarity of the profiles of EKE and pressure rms follows from the current approximate geostrophic balance. The larger relative magnitude of pressure at depth is attributed to a relatively larger contribution of small scale motions there. Rossby (Ro), Burger (Bu), and Rhines (R_β) numbers have been diagnosed in function of depth, from statistics of the simulation, as follows:

$$\mathrm{Ro}=f_0^{-1}\sqrt{\langle\xi'^2\rangle},\quad \mathrm{R}_\beta=\beta_0^{-1}\frac{\langle\xi'^2\rangle}{\sqrt{\langle U'^2\rangle}},$$

$$\mathrm{Bu}=\rho_0 g^{-1}N^2\sqrt{\frac{\langle w'^2\rangle}{\langle||\nabla_h\rho||^2\rangle\langle U'^2\rangle}}$$

where ξ is the vertical relative vorticity, w is vertical velocity, U is the horizontal velocity modulus, β_0 is the horizontal average of $\beta=\partial_f/\partial_y$, ∇_h states for the horizontal gradient modulus, prime denotes the deviation from the time mean (i.e., eddy-related component), and $\langle\rangle$ denotes horizontal and time averaging. Dependences on depth were not explicitly written for more clarity. Vertical averages of Rossby, Burger, and Rhines numbers are lower than 0.1, 0.75, and 10 respectively, which is a positive indication of QG validity.

3. True Fields

This study focuses mainly on 1 March 2008, from which true and reconstructed PV and pressure are inspected and compared. This section describes true PV and pressure fields, obtained from raw variables of the simulation, and labeled with the subscript *true*.

3.1. Pressure

True pressure p_{true} at −500 m (Figure 2a) reflects the GS presence with a pronounced meridional gradient perturbed by meanders and a rich eddy field including rings shed from the main current. Eddies of remote origin are also found in the southern part of the domain. At −1,500 m (Figure 2b), the strengths of the meridional gradient and of eddies are reduced compared to the −500 m level, consistently with the vertical profile of EKE (Figure 1b). Downstream, the pressure signal increases downward both due to the increase of mesoscale energy through deep cyclogenesis (Savidge & Bane, 1999) and the mean signal which contains a large-scale signature of stationary meanders (Figure 1a).

3.2. Potential Vorticity

At −500 m, the large-scale distribution of PV q_{true} (Figure 2c) is dominated by a meridional gradient across the GS which results from variations both of density and stratification between subtropical waters and waters found northward of the GS. At smaller scales, cold cyclones are bordered by an enhanced positive stripe which tends to delineate the sharpest gradients. An animated sequence (see movie in supporting information) shows than when GS meanders evolve into such cyclones, the stripe of positive PV at the core of the GS evolves into a ring, which is consistent with the conservation of PV under horizontal advection that characterizes the QG dynamics.

At −1,500 m, the sign of the large-scale meridional gradient is reversed (Figure 2d) compared to −50 m. At the mesoscale, PV is better correlated with pressure (see meanders of the GS Stream east of −66 W). The GS is at this depth a stripe of neutral PV instead of a highly positive PV stripe as at −500 m, which implies different gradients. By PV horizontal conservation, we can anticipate that any eddy shed by the GS, which has neutral PV, will be identified by a ring of neutral PV at −1,500 m. This is visible for the ring located at about −64.5°W, 34.5°N.

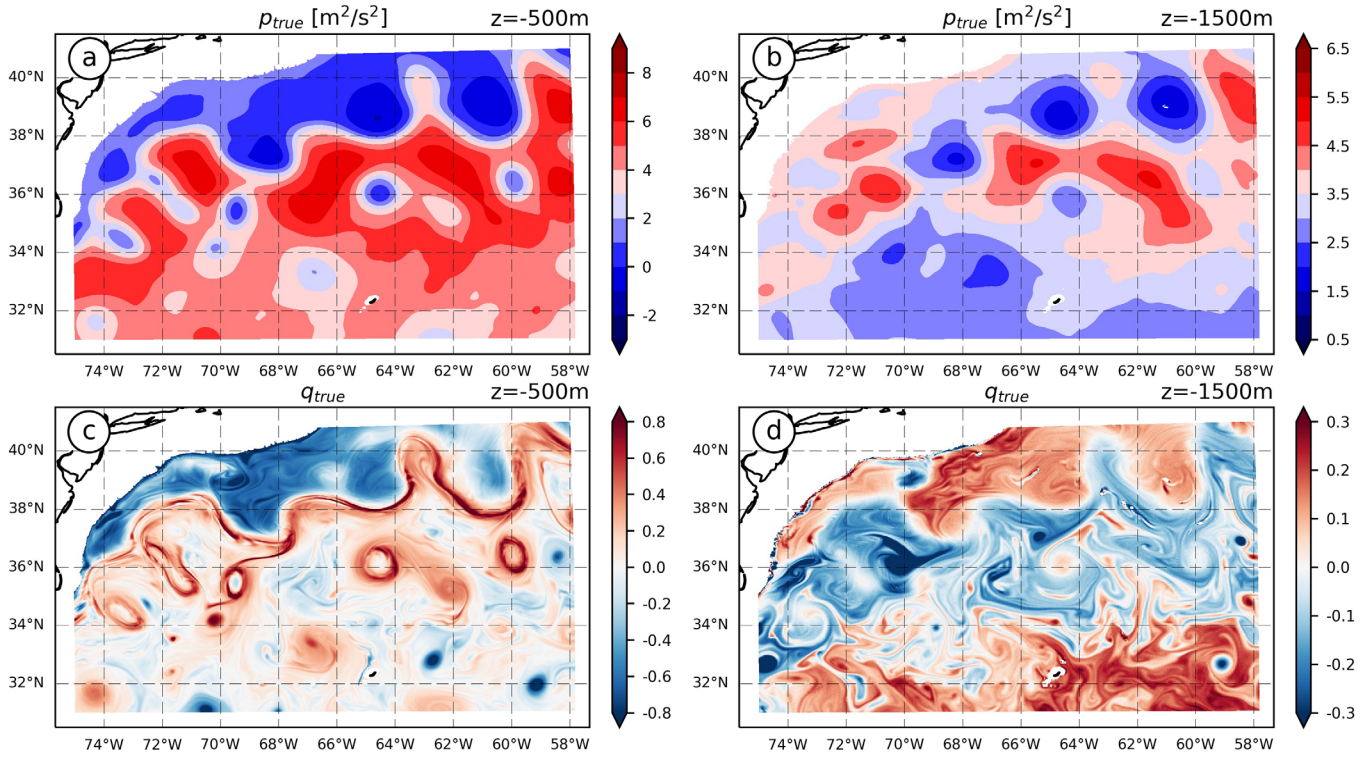

Figure 2. Horizontal sections at (left) −500 m and (right) −1,500 m of (a, b) p_{true} (unit: m^2/s^2) and (c, d) q_{true} (normalized by f_0). For the present and following figures (3–9), the date is 1 March 2008.

The structure of PV is finer horizontally and vertically compared to pressure, as expected from the relationship between these variables (equation (3)). These different spectral distributions between pressure and PV have an impact on correlations between PV and SSH (see section 4), and, on reconstructions of PV from SSH (see section 5 where energy spectra of PV and reconstructed PV will be compared).

4. Correlation Analysis

In order to identify the most relevant surface variables—among sea surface temperature (SST), sea surface salinity (SSS), sea surface density (SSD), and SSH—which can drive a skillful reconstruction of the 3-D dynamics, we perform in this section a time correlation between the 3-D fields of pressure and PV and (1) a single level of the same variable (autocorrelation) and (2) the surface variables. Autocorrelations indicate the degree of vertical coherence of these variables and will be used as background information in discussions about correlations between pressure and PV, and surface variables.

4.1. Autocorrelation of Pressure and PV

Horizontally averaged vertical autocorrelation of pressure was computed for several reference levels (Figure 3a). The pressure signal is highly autocorrelated below −1,500 m but these deep levels are only weakly correlated with surface levels. Above −1,000 m, the vertical extent of autocorrelation is smaller than at depth: correlation with the −200 m level decreases to 0.82 both at surface and at −1,000 m, and correlation with surface decreases to 0.6 at −1,000 m. The vertical autocorrelation of pressure does exhibit geographical variations though. This is illustrated by a vertical section at −65°W of the correlation with surface pressure (Figure 3b) whose vertical extent is maximum in the vicinity of the GS (correlation >0.8 reaches the −3,500 m level at 38°N) but decreases southward (correlation >0.8 do not reach the −100 m level at 31°N). This peak of correlation varies also along the GS path and has a maximum downward penetration east of −68°W (not shown). This is consistent with the scenarios of deep circulation generation following the steepening of GS meanders (Savidge & Bane, 1999; Shay et al., 1995; Watts et al., 1995) but is at odds with the results of Meinen and Luther (2016) about the decoupling of the circulation in the vertical over the GS. Savidge (2016) discusses

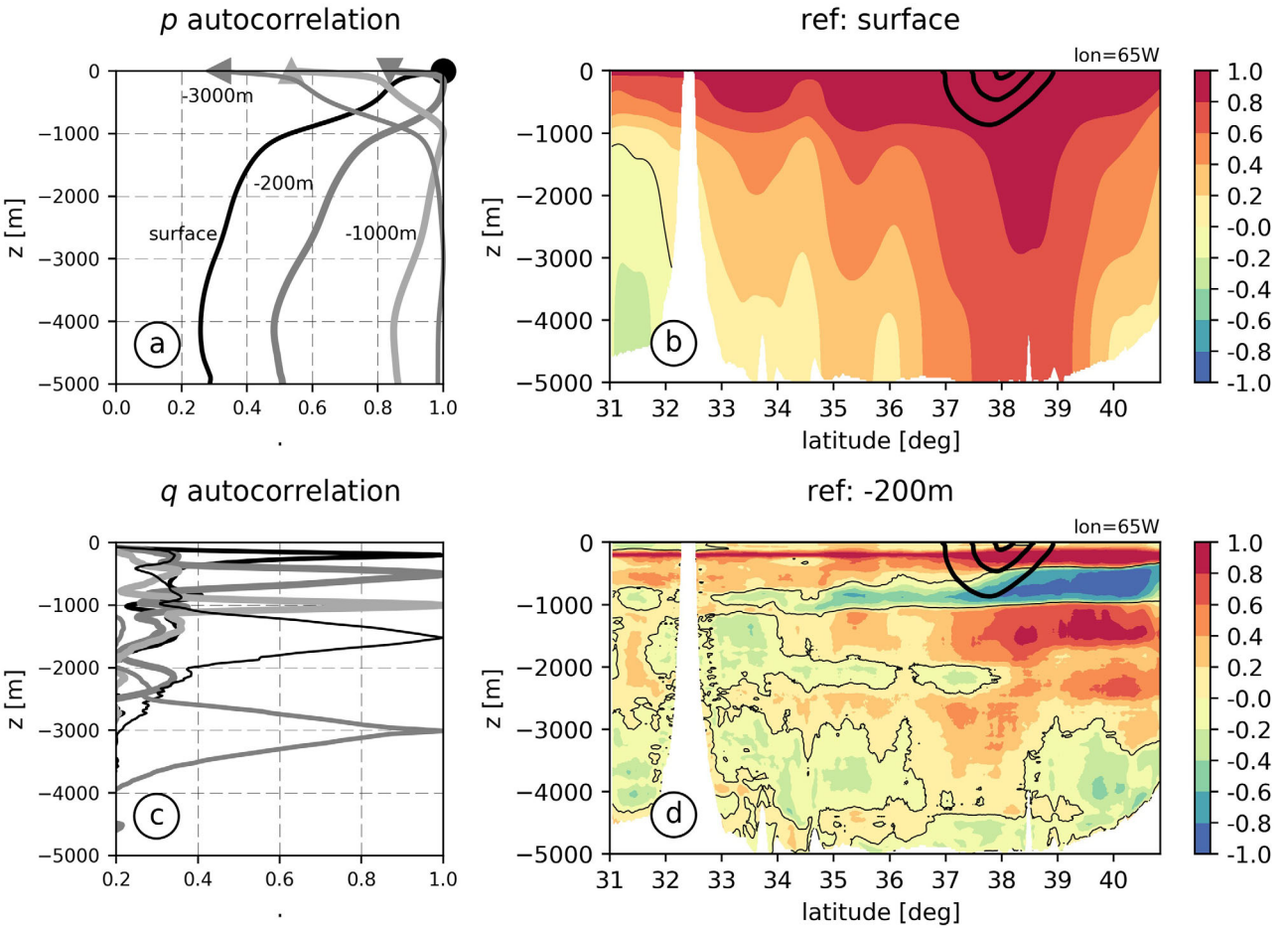

Figure 3. Autocorrelation vertical profiles of (a, b) pressure and (c, d) PV. (left) Horizontal average for several test levels: (a) surface, −200, −1,000, and −3,000 m (see labels) and (c) −200, −500, −1,000, −1,500, and −3,000 m (in the order of curves reaching autocorrelation = 1). (right) Vertical section at −65 W overlaid with the current velocity time mean (thick line, interval: 0.2 m/s) of (b) pressure autocorrelation with the surface reference and (d) PV autocorrelation with the −200 m reference. In Figure 3a, symbols mark the value of autocorrelation at the surface level.

particularities of Meinen and Luther (2016)'s analysis that may explain this discrepancy. The higher level of correlation over the GS is an opportunity for the reconstruction of the ocean dynamics from SSH.

PV is much less autocorrelated in the vertical direction than pressure (Figure 3c): this result is linked to the complex structure of PV on the vertical (Figures 2c and 2d). In particular, for numerous GS rings, some levels display a core-shaped PV anomaly while other levels display a ring-shaped PV anomaly. This structural difference does not favor high pointwise vertical correlation despite colocalization of the anomaly centers. The GS isolates water masses with more important autocorrelations (sign ignored) on its northern side (Figure 3d) which demonstrates that the autocorrelation varies geographically and may be enhanced locally.

4.2. Correlation Between Pressure and Surface Variables

Pressure anomalies are weakly correlated with SST, SSS, and SSD anomalies throughout the water column (values are lower than 0.6; Figure 4a). As expected, pressure is perfectly correlated with SSH at the surface and remains more strongly correlated with SSH than with SST, SSS and SSD in the upper 1,000 m of the water column.

Correlations between SSH and subsurface pressure are larger in the vicinity of the GS (Figure 5e), as expected from autocorrelation of pressure (Figure 3b). Correlation with SST or SSS has a first local maximum within the GS and more suprisingly within Sargasso Sea at some distance from the GS (Figures 5a and 5c). This second local maximum is homogeneous on the water column below −1,000 m (supporting information Figure S1). The latter result is not trivial since we do not expect a physical phenomenon which

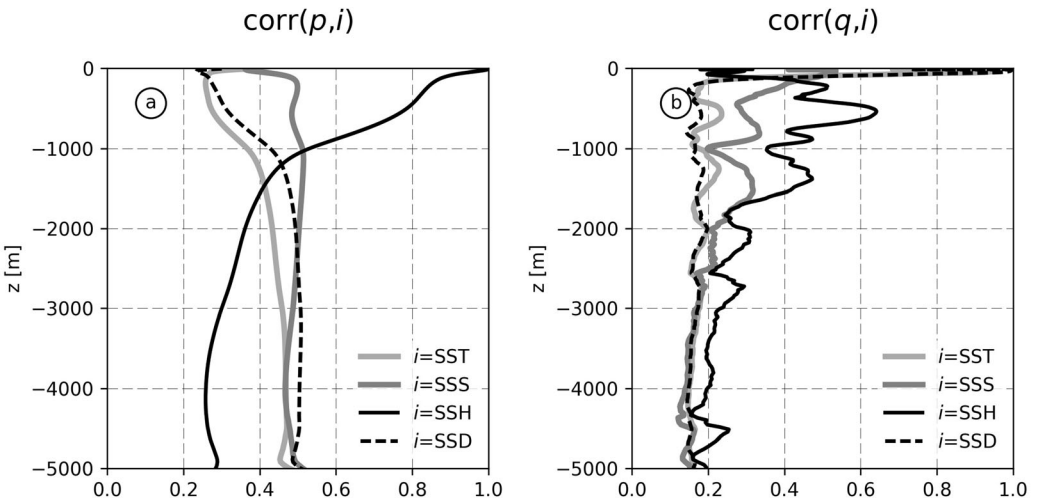

Figure 4. Horizontally averaged vertical profiles of the correlation coefficient of (a) pressure and (b) PV with SST (plain, light gray), SSS (plain, dark gray), SSH (plain, black), and SSD (dashed, black).

correlates the whole column with surface tracer anomalies. Temperature at 200 m depth does not actually exhibit such correlation (supporting information Figure S2). Additional diagnostics show that, within this region, the rms of pressure below −1,000 m is dominated by seasonal variations of the mixed layer weight which is a nonrealistic result due to the absence of steric compensation in the numerical model, i.e., the seasonal variability of surface density affects pressure at depth but not SSH. In a non-Boussinesq model, the correlation between pressure below −1,000 m and SST is expected to disappear (Mellor & Ezer, 1995).

Correlations with SSD are almost equivalent to correlations with SST with a reverse sign, both regarding the spatial average (Figure 4a) and the 3-D spatial distribution (supporting information Figure S1).

4.3. Correlation Between PV and Surface Variables

PV is not well correlated with surface variables except at the surface with SST and SSD (Figure 4b). The latter is explained by the fact that seasonal SST and SSD variations are strongly linked to seasonal variations of stratification which dominate PV surface fluctuations through the stretching term (not shown). Away from the surface, largest correlations are found with SSH (e.g., up to 0.6 at −700 m). The overall weak correlation between PV and surface variables is consistent with the limited extent of PV vertical autocorrelation (Figure 3c). Given the relationship between pressure and PV (3), the linear estimation of PV from SSH associated with these correlations is also not expected to be successful across all wave numbers.

At 500 m depth, the mean GS position seems to be a boundary for correlations between PV and surface variables (Figures 5b, 5d, and 5f), as already observed for PV autocorrelations (Figure 3d). On the northern side of the mean GS position correlations are positive (highest for SSH), whereas they are negative (SSH and SST) or low (SSS) on the southern side. A lagrangian perspective on the basis of Figure 2c (see also supporting information movie) provides insight on this result. On the northern side of the mean GS position, the sign of correlations is consistent with the advection of the mean meridional gradients of interior PV and surface variables by meanders and eddies. For example, a warm anticyclone propagating north of the GS brings anomalously high PV northward and manifests itself with anomalously high SSH, SST, or SSS. On the southern side of the mean GS position on the other hand, the cyclonic variability is dominated by cyclonic eddies (cold rings) that have detached from the GS. The process by which a GS meander evolves into a cyclonic eddy occurs over short distances so that little cold water with negative PV, as found north of the GS, is entrained within the eddy. The eddy is then characterized by neutral PV at its center surrounded by a ring of positive PV as found in the core of the GS. Additionally, anticyclonic eddies of remote origin and characterized by negative PV dominate the anticyclonic variability. The combination of both of types of variability may explain the negative correlations between PV and surface variables found south of the mean GS position.

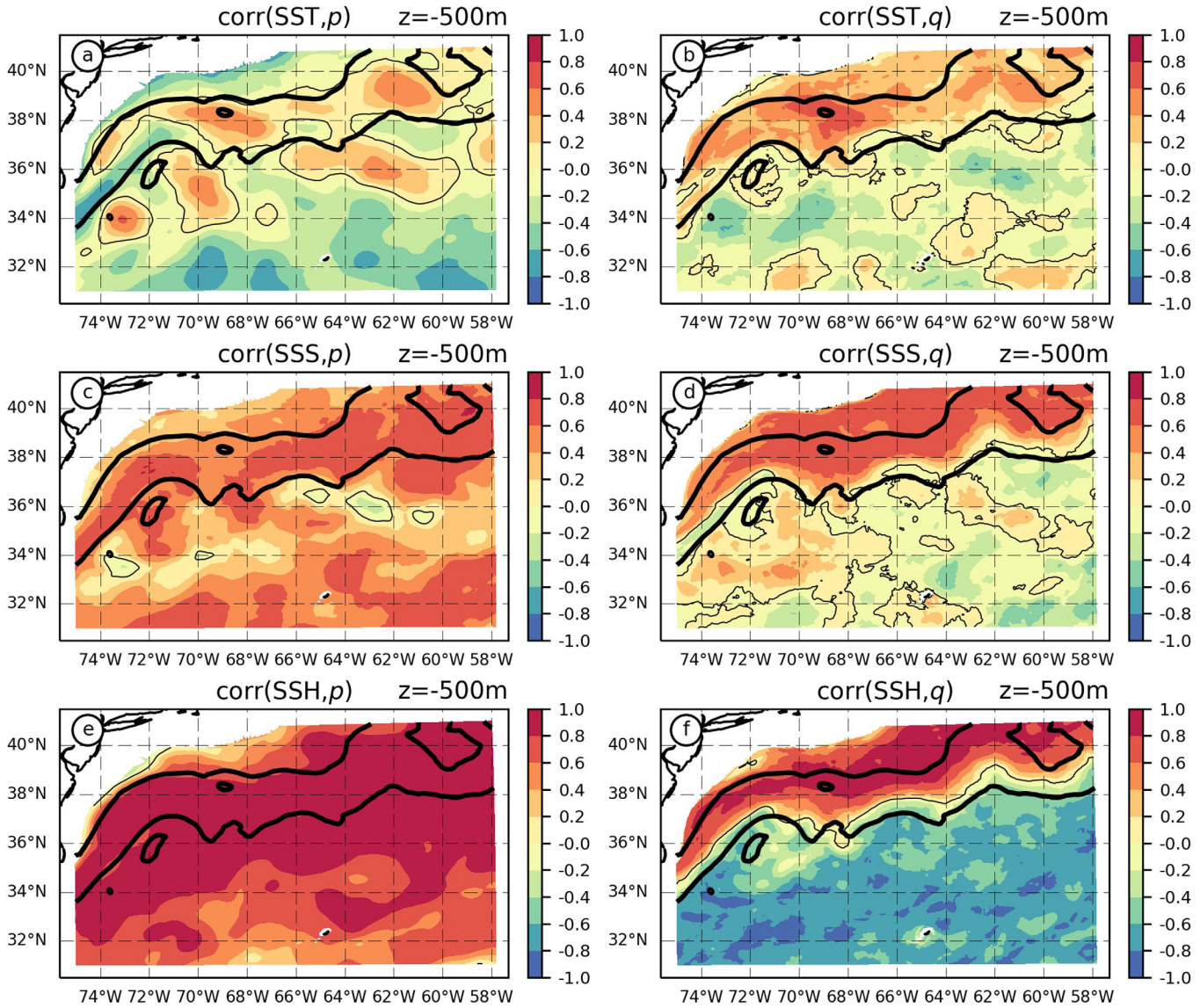

Figure 5. Horizontal sections at −500 m of the correlation coefficient of (left) pressure and (right) PV with (a, b) SST, (c, d) SSS, and (e, f) SSH, overlaid with the line 0.2 m/s of the surface current time mean.

5. Reconstruction of the 3-D Pressure and QGPV Fields

Given that SSH is overall more highly correlated with pressure and PV than SST and SSS, SSH will be used next to reconstruct pressure and PV assuming a linear relationship. In the following, we present the results of a single test date, 1 March 2008, from which true fields were previously detailed (see section 3), but we point out that most of the results seem to be valid at any date (see section 6.4), with no evident seasonal variation.

5.1. Presentation of the Experiments and Skill Metrics

Pressure and PV reconstructions are achieved assuming a linear relationship with SSH. For pressure for example, the reconstruction is given by

$$p'_{reg}(x,y,z,t)=\alpha(x,y,z)\mathrm{SSH}'(x,y,t) \tag{5}$$

where $\alpha(x,y,z)$ is the regression coefficient between pressure and SSH, computed from the 2 years of data and prime denotes the deviation to 2 year mean. Overview of the reconstruction is shown at the −500 and −1,500 m levels (Figures 6a, 6b, 8a, and 8b).

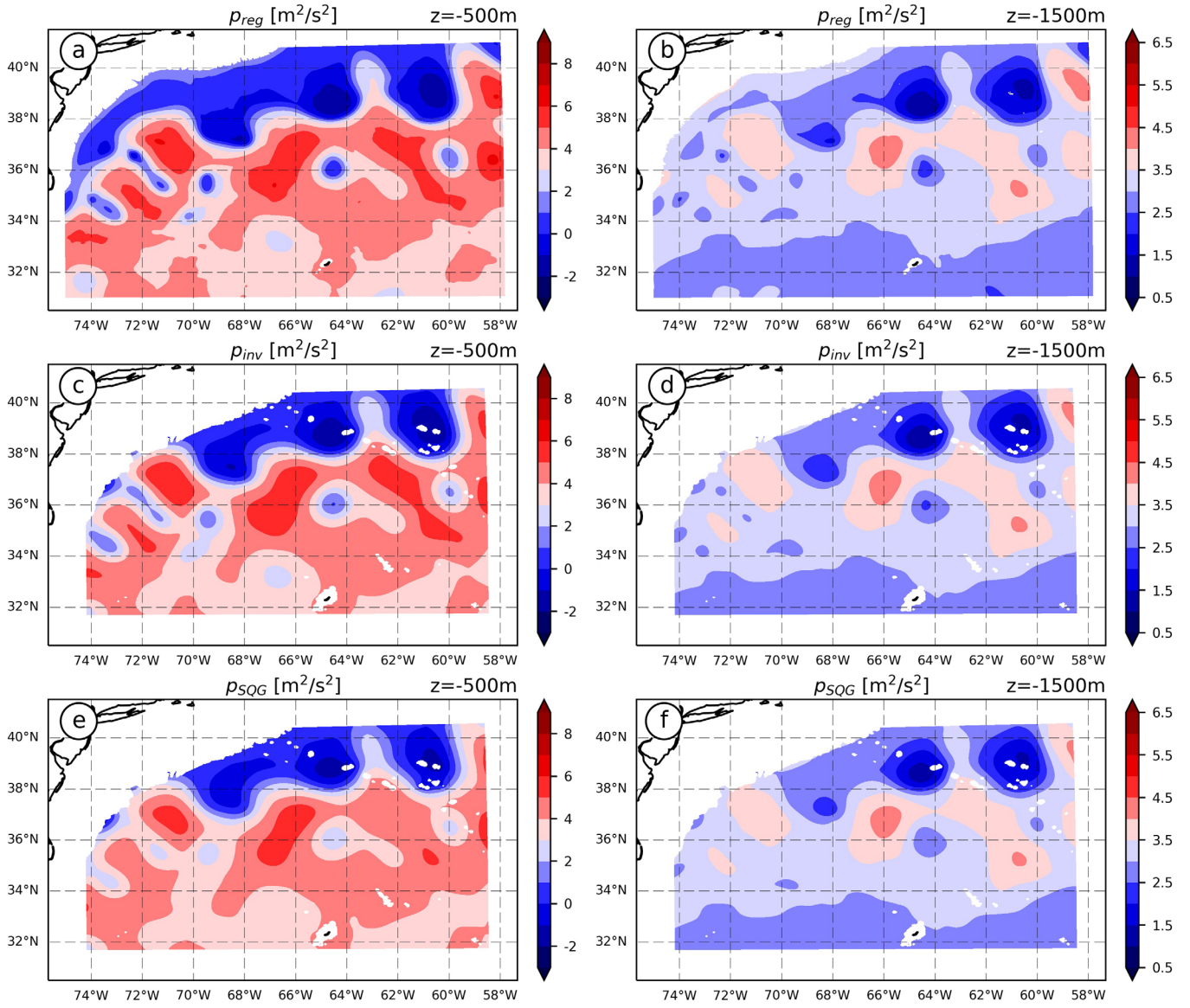

Figure 6. Horizontal sections at (left) −500 m and (right) −1,500 m of pressure reconstructions (a, b) p_{reg}, (c, d) p_{inv}, and (e, f) p_{SQG}. Units: m^2/s^2.

The root-mean-square difference between the 2 year mean (labeled as *clim*) and the true pressure fields is chosen as an upper bound for the acceptable error, i.e., a no-skill threshold. A reconstruction associated with an error close to this upper bound would mean that the knowledge of surface anomalies does not yield, on average, a better reconstruction than climatology.

We define for each reconstruction i and depth z a skill score:

$$S(i,z)=\max\left(\frac{\mathrm{RMSE}(clim,z)-\mathrm{RMSE}(i,z)}{\mathrm{RMSE}(clim,z)},0\right)$$

where RMSE stands for the horizontal rms deviation to true fields. S values lie between 0 (no skill) and 1 (perfect skill). Using the 2 year mean, the no-skill threshold corresponds to a pressure RMSE between 60% ($z=0$ m) and ≈100% ($z=-3{,}000$ m) of the true rms and a PV RMSE between 50% and 100% of the true rms over the 200–3,000 m depth range.

5.2. Reconstruction of *p*: Linear Regression

At both 500 and 1,500 m depths, the linear regression of pressure on SSH p_{reg} places most of the patterns present in the true pressure field at the right places (Figures 6a and 6b). Cold-core cyclones have the right

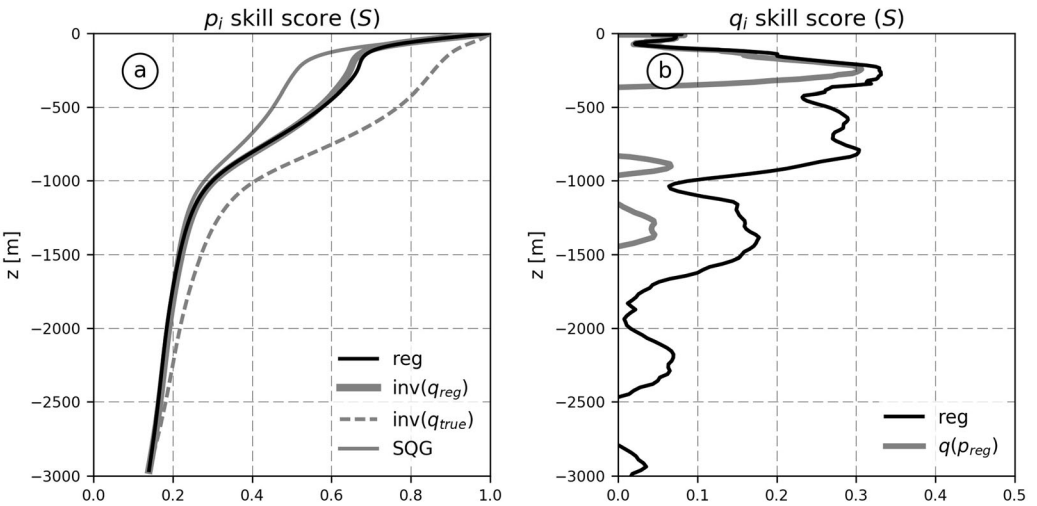

Figure 7. Vertical profile of the skill score S of (a) pressure and (b) PV reconstructions. See text for the definition of S. Pressure reconstructions are p_{reg} (black), p_{inv} (thick, gray), inversion of q_{true} (dash, gray), and SQG (plain, gray). PV reconstructions are q_{reg} (black) and $q(p_{reg})$ (gray) (negative values of S were hidden).

magnitude at 500 m depth. Reconstructed amplitudes of anticyclonic structures south of GS crests and within eddies are underestimated, while reconstructed amplitudes of cyclonic structures within GS troughs are larger than actual ones. At 1,500 m depth, the amplitude of all features but cyclonic structures within GS troughs are underestimated, with a skill visually increasing in the downstream direction. The reconstruction overall captures more features nearby the GS, as expected from the structure of the correlation coefficient (Figure 5e and section 4.1). The enhanced loss of skill in the upper 200 m and between −500 and −1,000 m (Figure 7a) is consistent with the statistical decorrelation rate between SSH and pressure (see section 4.3).

5.3. Reconstruction of q: Linear Regression

Linear regression of PV on SSH (Figures 8a and 8b) yields smoother fields than truth (Figures 2c and 2d), in consistency with the relationship between surface pressure, a posteriori SSH, and PV (equation (3)). An inspection of wave number spectra (Figure 9) indicates that the reconstruction of PV from SSH largely inherits its spectral shape, which is steeper than that of the actual enstrophy. While the reconstructed enstrophy of most energetic scales is well predicted, higher wave numbers are thus underestimated.

Nonetheless, linear regression does not operate as a simple low-pass filter applied on the true fields. The stripes of positive PV that characterized the GS and cold-core cyclones at −500 m (Figure 2a) are replaced by a gradual transition from positive values at the core to weakly negative ambient ones (Figure 8a). Furthermore, the PV of anticyclonic eddies in the southern part of the domain is largely underestimated while cyclonic eddies which do not have a ring structure are well reconstructed (these eddies are of remote origin, see supporting information movie).

Linear regression applied to PV has a rather low skill compared to pressure (Figure 7b), when averaging results on the horizontal dimension. On average, depths with a slightly significant skill ($S > 0.2$) are located over the 200–1,000 m range. The low skill in the upper 200 m may be due to the non-QG dynamics within the surface mixed layer.

5.4. Inversion of q_{reg} and SQG-Like Reconstruction

The last two reconstructions of pressure consist in inverting q_{reg} given $p_{surface}$, yielding p_{inv} and in inverting $p_{surface}$ with zero PV anomaly, i.e., a SQG-like experiment, yielding p_{SQG}. The latter reconstruction aims at gauging the weight of PV versus that of the surface boundary condition in the reconstruction of pressure. The surface boundary condition used in both inversions is to impose the value of the stream function provided by SSH. The inversion domain is chosen to reconstruct pressure between surface and −3,000 m, the bottom level being chosen in order to avoid numerous intersections with bathymetry. Details of the procedure may be found in Appendix A.

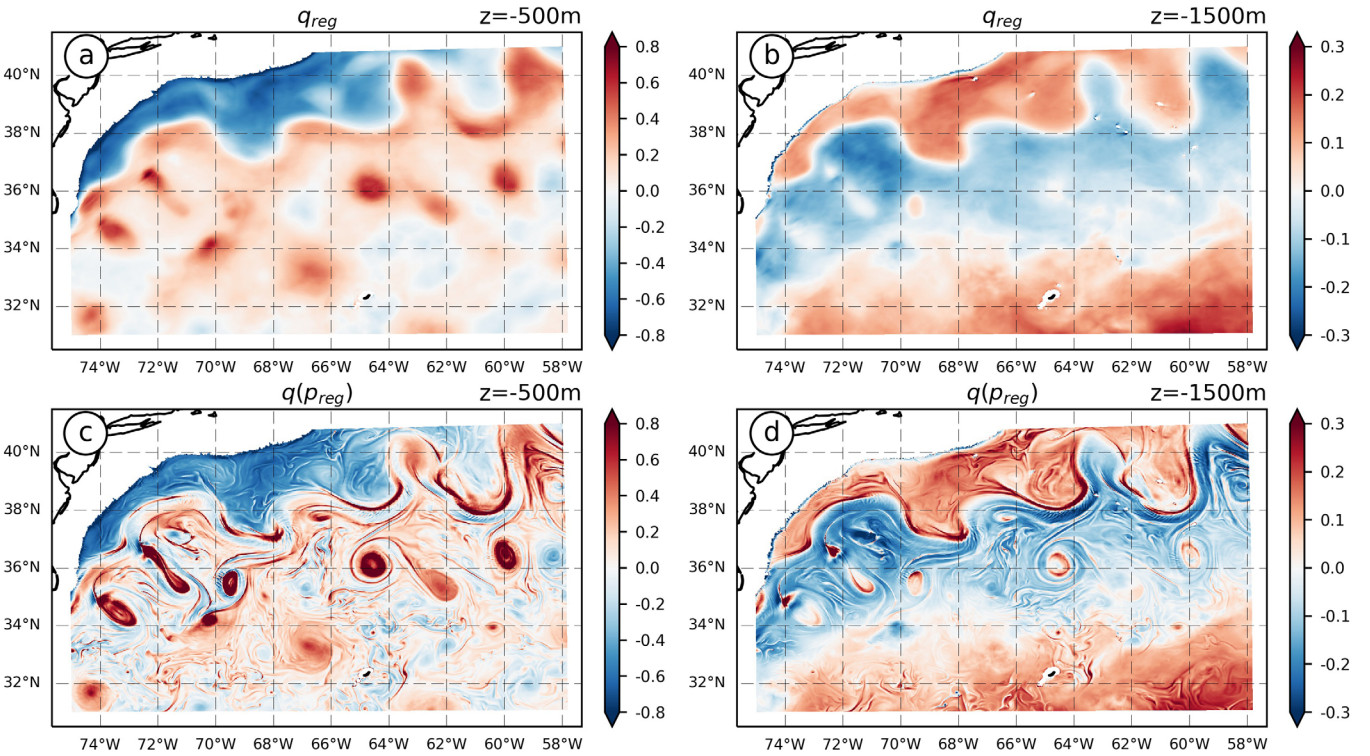

Figure 8. Horizontal sections at (left) −500 m and (right) −1,500 m of PV reconstructions (a, b) q_{reg} and (c, d) $q(p_{reg})$. All variables are normalized by f_0.

Patterns of p_{inv} and p_{reg} at the two depths (500 and 1,000 m) are visually identical to that from a linear regression (compare Figures 6a–6d) and the skill score $S(p_{inv}, z)$ overlays almost perfectly $S(p_{reg}, z)$ (Figure 7a). In comparison, the SQG reconstruction p_{SQG} shares similar patterns but these are further weakened compared to p_{inv} and p_{reg} (Figures 6e and 6f). Its skill score is slightly degraded over the 200–1,000 m depth range compared to the latter reconstructions, by about 0.15 at −500 m (Figure 7a). The three reconstructions have overall a comparable skill nonetheless, suggesting that the reconstruction of pressure by QG inversion is here dominated by the boundary conditions and that PV estimations from SSH are not sufficiently accurate to improve reconstructions significantly.

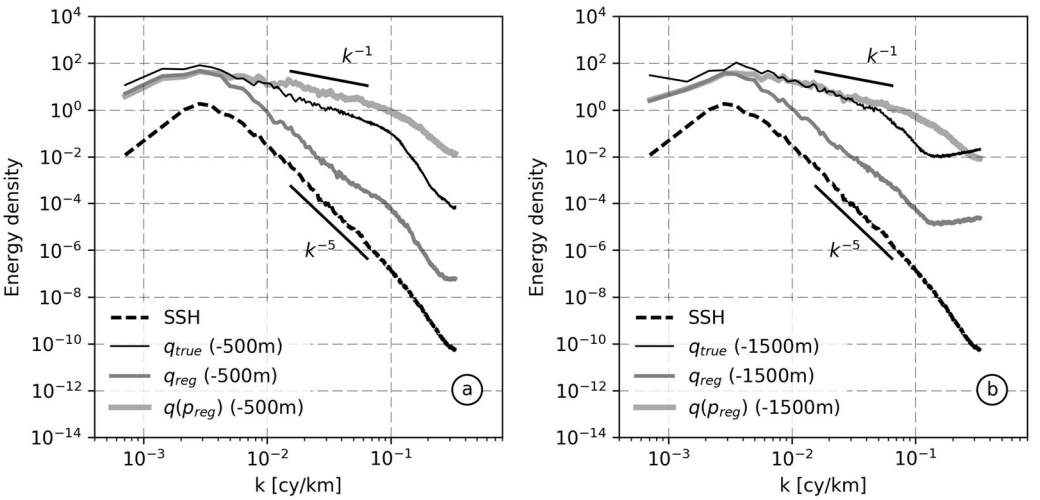

Figure 9. Energy density spectrum of q_{true} (thin lines), q_{reg} (midthickness lines), and $q(p_{reg})$ (*thicklines*) at (a) −500 m and (b) −1,500 m, overlaid with the SSH energy density spectrum (dashed line). Arbitrary units. Respective energy of all PV variables may be compared.

6. Discussion

6.1. Role of the Mixed Layer Dynamics

Why are surface tracers (e.g., SST, SSS) less correlated with pressure and PV than SSH? Assumptions of quasi-geostrophy and of weak current baroclinicity would indeed favor a linear relationship between anomalies of PV and surface tracers (Lapeyre & Klein, 2006, Appendix B). Mixed layer dynamics and air-sea exchanges may constitute a buffer that blurs the link between the interior ocean dynamics and its surface manifestation. This hypothesis is confirmed by correlations between temperature at 200 m depth, and, pressure and PV (see supporting information Figures S1 and S2). These correlations indeed indicate that temperature below the mixed layer is as well correlated with pressure and PV than SSH.

6.2. Comparison of the Reconstruction Skill Between Pressure and PV

We have shown that above −1,000 m, PV reconstruction skills (Figure 7b) are much lower than pressure reconstructions (Figure 7a). Several reasons contribute to this result. One is that the reconstructed PV has a steeper spectrum than the actual PV (Figure 9), which prevents from a low RMSE and consequently large values of S. Second, the weight of small scales structures is larger in correlations involving PV while these structures are more likely to be incoherent vertically, hence faster vertical decorrelations compared to pressure and poorer correlations with surface variables.

Does the reconstruction of pressure from direct linear regression on SSH produce correct PV distributions? To provide an answer, the operator defining PV (see Appendix A, equation (A1)) is applied on p_{reg}, yielding $q(p_{reg})$, and compared with the result of the regression between PV and SSH q_{reg} (compare Figures 8a–8d). Eddies and meanders are reproduced in both fields. More fine scale features are found in $q(p_{reg})$ but these are not correctly located or not of the good sign (see for example the GS core). An exception may be in cold-core cyclones where a minimum of PV is found at the core with $q(p_{reg})$ which is an improvement compared to q_{reg}. In terms of spectral distribution, $q(p_{reg})$ is closer to actual PV compared to q_{reg} and its spectrum is slightly whiter than the actual PV spectrum (Figure 9). The spectrum of the difference $q_{true}-q(p_{reg})$ is almost similar to the spectrum of $q(p_{reg})$, being the evidence that $q(p_{reg})$ does not have the right phase and amplitude at all scales. We thus conclude that apart from containing a more realistic amount of fine scale features, $q(p_{reg})$ does not represent a useful reconstruction of the ocean circulation.

6.3. Spectral Analysis of the Skill

We investigate here how reconstructions perform in horizontal wave number space. The metric chosen is the squared spectral coherence $C^2(k,z)$, which is computed as a function of depth z and horizontal wave number k (in cy/km). $C^2(p_{true},p_{reg})$ (Figure 10a) shows that p_{reg} is successful in estimating the actual pressure field for wavelengths between 100 and 500 km. By construction, the coherence is approximately 1 at surface for all wavelengths (given the relationship between $p_{surface}$ and SSH) and a rapid transition happens within the first 100 m from a wide wave number window of higher skill to a restricted one at depth. An important skill (chosen arbitrarily as $C^2 > 0.95$) is found in the 200–600 km range of wavelengths at −200 m but disappears for levels deeper than −700 m. We choose arbitrarily the 0.75 value to define a depth of critical skill $D_c(2\pi/k)$ below which reconstructions are not skillful anymore at a given wavelength: D_c (200 km) ≈ 800 m, D_c (100 km) ≈ 250 m, and D_c (50 km) ≈ 200 m. The qualitative distribution of coherence resembles that of the spectral correlation between surface and interior relative vorticity in Isern-Fontanet et al. (2008) and Klein et al. (2009).

The skill of p_{inv} and p_{SQG} projects almost exactly onto the same wavelengths and the same skill critical depths may be estimated. This result suggests that the spectral reconstruction by QG inversion is dominated by the surface boundary condition and confirms that even a crude, in terms of correlation and spectral distribution, approximation of PV such as q_{reg} may be sufficient to reconstruct a pressure field close to a direct regression on SSH, provided the following boundary conditions: p_{true} at the surface and p_{reg} on lateral and bottom boundaries.

6.4. On the Robustness of the Results

In order to provide some indication on the robustness of previous results, we have repeated exactly the same exercise for the first day of June, September, and December 2008, forming eventually a regularly spaced four-member sample of a 1 year period. Results show that despite a signature of seasonal variations on the absolute value of scores, the following statements are conserved: the horizontally averaged skill of

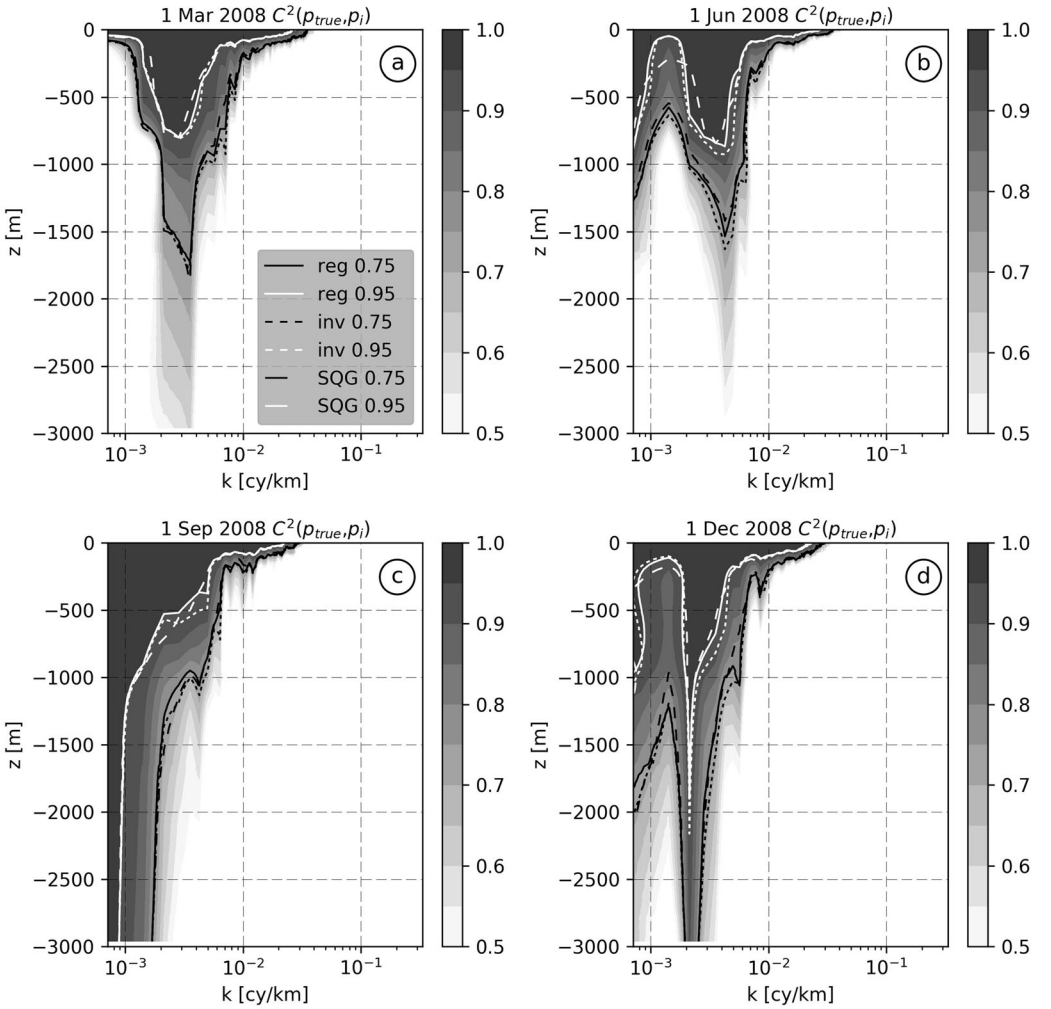

Figure 10. Vertical profile of spectral coherence $C^2(p_{true}, p_{reg})$ (shaded) in function of the normalized wave number k, overlaid with the lines 0.75 and 0.95 of $C^2(p_{true}, p_{reg})$ (plain line), $C^2(p_{true}, p_{inv})$ (short dash), and $C^2(p_{true}, p_{SQG})$ (long dash). Dates are (a) 1 March 2008, (b) 1 June 2008, (c) 1 September 2008, and (d) 1 December 2008.

reconstruction is almost similar between p_{reg} and p_{inv} (not shown); p_{SQG} is less skillful between −150 and −500 m but as skillful at other depths (not shown); the 0.75 line of squared coherence and the skill critical depth at 100 km wavelengths is almost similar among the three experiments (Figure 10). We suggest therefore that methods presented in this article have robust differences and similarities.

Reconstructions based on PV inversion showed little sensitivities to the choice of the reference density profile and the size of the domain for inversions (not shown). The reference density profile is expected to impact the actual conservation of PV upon horizontal advection which may in turn affect the relationship between observable surface variables (e.g., SSH, SST, and SSS) and PV (see Appendix B). The lack of sensitivity to the reference profile is thus interpreted as a sign of the poor estimation of PV and its low weight in the quality of reconstructions.

6.5. Operational Applicability

In order to apply the methods proposed here to a real case scenario, one will need to estimate correlations between pressure or PV and SSH. A combination of the Argo and the altimetric data sets may allow computations of the pressure-SSH correlations in a fashion similar to (Guinehut et al., 2006, 2012). The same combinations may also work in order to estimate correlations between PV and SSH, since these correlations are dominated by motions at scales where stretching dominates and since stretching may be estimated from

Argo profiles. Even though not shown, we verified indeed that regression coefficients between PV and SSH and regression coefficients between the PV stretching term and SSH are similar.

A spatiotemporal variability of pressure-SSH or PV-SSH correlations may complicate the applications of the methods considered here if the space and time scales of this variability are smaller than those imposed by the density of the observational network in order to estimate these correlations. We have not investigated here the effects of such variability but this could be done with an analysis of a longer numerical simulation, or with an analysis of actual observations (Argo and altimetry combined) which span now more than a decade. Another interesting prospect which could mitigate the impact of a variability of these correlations would be to relate the ocean large-scale hydrography to correlations coefficients. Such relationships were physically motivated by Lapeyre and Klein (2006) and partially verified with a realistic numerical simulation by Lapeyre (2009). The assumption here is that this large-scale hydrography is easier to be estimated from observations than correlations with surface variables.

We have also not estimated the ability of the present-day observational network (Argo plus altimetric constellation) at estimating these correlations. Regarding pressure-SSH correlations for example, we know from Guinehut et al. (2006, 2012) that there is enough information in order to estimate these correlations but an interesting question could be: what is the minimal amount of information required to do so?

Pushing further, one may wonder whether reconstructions could be carried with surface observations only. Several methods have been proposed already: SQG reconstructions (Isern-Fontanet et al., 2008; Lapeyre & Klein, 2006), reconstructions based on a priori distribution on vertical dynamical modes in combination or not with SQG (Wang et al., 2013). All require some knowledge of the stratification at least. As shown here though, including information about the statistical link between surface variables and interior ones does improve reconstructions, albeit modestly (Figure 7a).

7. Conclusion

We have investigated the statistical relationship between the surface variables (SST, SSS, and SSH) and pressure and PV at depth in a 2 year high-resolution simulation of North Atlantic over the Gulf Stream region and compared several methods of reconstruction of the pressure and PV based on the former statistics. Domain-averaged correlation between pressure and SSH, which is by construction perfect at the surface, decreases rapidly in the upper 1,000 m of the water column. Pressure is more highly autocorrelated in the vertical direction in regions neighboring the Gulf Stream where high correlations ($>$0.8) reach levels down to 3,000 m depth. PV decorrelates more rapidly in the vertical direction and is less correlated with surface variables than pressure. Pressure and PV are more highly correlated with SSH than with SST or SSS which motivated the use of SSH in order to estimate these variables. This hierarchy is characteristic of surface variables. Indeed, selecting temperature at levels below the mixed layer yields a correlation resembling to the one obtained with SSH (including a high correlation with pressure at depth in the vicinity of the GS, see supporting information Figure S1). Future work will investigate whether preprocessing of SST and SSS (via spatial high-pass filtering for example) may mitigate the noise induced by mixed layer dynamics and air-sea fluxes and improve correlation with pressure and PV.

The knowledge of SSH allowed valuables and comparable reconstructions of the 3-D pressure field whether they are based on a direct linear relationship between pressure and PV, or on the inversion of PV estimated from SSH, or on an inversion with no PV (SQG-like). For all levels above $-$1,000 m, reconstruction skill scores are greater than 60% of the no-skill RMSE associated to a temporal average. Over the 250–1,000 m depth range, the three reconstructions of pressure are skillful at wavelengths between 500 and 200 km. The loss of skill between 100 and 200 km wavelengths corresponds to a 600 m rise of the depth of critical skill. Reconstructions based on PV inversion are only modestly improved when PV anomalies reconstructed from SSH is used instead of assuming zero PV anomalies. This emphasizes that estimating PV from SSH via a linear regression does not yield a PV field that is sufficiently accurate in order to improve reconstructions of the 3-D pressure field. Future work will investigate whether more advanced statistical techniques may account for the nonlinear relationship between PV and SSH and/or combine information from other tracers (e.g., SST/SSS, see Assassi et al., 2016 for example) in order to improve the quality of the PV estimate.

Applicability of the present approach to other regions remains to be verified. Gulf Stream eddies are energetic and extend over most of the water column which explains the good correlations found between SSH and pressure at depth and justifies the relevance of methods leveraging these correlations in this area. Preliminary results south of the Azores Front and over the Reykjaness Ridge suggest that correlation between pressure or PV and surface variables are likely to be lower in less energetic regions.

The similarity of the pressure reconstruction skill between a method using PV and a method purely statistical proves that the QG framework is relevant to design valuable methods of reconstruction of the dynamics. A major source of improvement of these reconstructions lies in the predictive ability of the QG framework for mesoscale features (Ubelmann et al., 2015, 2016) which should be quantified and leveraged in future studies. We could also extend the skill of the QG framework to reconstruct QG vertical velocities which are a good approximation of the true mesoscale vertical velocities if pressure is reconstructed with enough accuracy.

Appendix A: Inversion of q_{reg}

The compact definition of the quasi-geostrophic potential vorticity (see equation (3) in section 2.2) is

$$q = L\psi \tag{A1}$$

where ψ is the geostrophic stream function and L is an elliptic operator containing the domain-averaged Coriolis parameter f_0 and the reference profile of squared Brunt-Vaisala frequency $N^2(z)$.

Inverting q_{reg} is to solve (A1) for ψ (or equivalently the pressure $p=\psi/f_0$) with the constraint $q=q_{reg}$ over a domain D of the model grid, with appropriate boundary conditions.

The code performing the inversion is available on https://github.com/apatlpo/qgsolver.

The construction of D is detailed as follows. We first consider a 3-D square domain of size $N_x N_y N_z$. The square is chosen to be slightly smaller than the Gulf Stream domain on the horizontal dimension, reduced by 50 points on each side, in order to allow optimal parallel processing. On the vertical dimension, the square extends from the surface level to $-3{,}000$ m only, in order to reduce the area of the bathymetric intersection of the bottom level. From this bottom level, we define a 2-D mask: $M(x,y)=1$ at a sea point and 0 elsewhere. D is defined as the 3-D square domain removed from the points $M(x,y)=0$ at each depth. Therefore, every lateral face of D is a vertical wall extending from the surface to $-3{,}000$ m.

Boundary conditions are chosen according to the fact that we know the true pressure at surface and an estimation p_{reg} (see section 5.2) in the vicinity of all other boundaries. Using the Dirichlet condition, boundary conditions write

$$\begin{aligned} p &= p_{true} \quad \text{at } z=0 \text{ m}, \\ p &= p_{reg} \quad \text{at } z=-3,000 \text{ m}, \\ p &= p_{reg} \quad \text{on lateral walls} \end{aligned}$$

The choice of the bottom condition is driven by additional inversion tests, which have shown that p_{reg} (–3,000 m) propagates smaller RMSE to the solution than $\partial_z p_{reg}$ (–3,000 m).

Appendix B: Dynamics Versus Statistics in Reconstructions From Surface Variables

B1. Dynamics

Dynamical ingredients have been employed in order to justify reconstruction strategies. The piling of energy at the first baroclinic mode that is explained dynamically by the weak energetical transfers to the barotropic mode in the presence of a pycnocline (Smith & Vallis, 2001) may motivate for example a reconstruction based on the extrapolation of altimetric observations assuming a first baroclinic mode vertical structure. Alternatively and under the assumptions that (1) the vertical shear is weak in the upper part of the water column, (2) there are well-defined large-scale meridional gradients of PV $\bar{q}$ and of a conservative surface tracer $\bar{\theta}_s$, and (3) these gradients are uniform horizontally, dynamical arguments similar to those of Lapeyre and Klein (2006) suggest that PV anomalies q' at depth may be related to those of the surface tracer according to

$$q'(x,y,z,t)=\alpha_{q,\theta_s}(z)\theta'_s(x,y,t) \tag{B1}$$

with

$$\alpha_{q,\theta_s}(z)=\partial_y\bar{q}/\partial_y\bar{\theta}_s \tag{B2}$$

Assuming PV is dominated by its stretching term (see last term in the RHS of equation (4)), as it occurs for scales larger than the internal Rossby radius of deformation and if baroclinic contributions dominate barotropic ones:

$$q'(x,y,z,t) \sim \partial_z\left(\frac{f_0^2}{N^2}\partial_z\psi'\right) \tag{B3}$$

A double vertical integration of (B3) between a level ($z=-H$) of no flow ($\psi'=0$) and no density anomalies ($\partial_z\psi'=0$) along with (B1) leads to

$$\mathrm{SSH} \sim \left(\int_{-H}^{0}\frac{N^2}{gf_0}dz\int_{-H}^{z}\alpha_{q,\theta_s}dz'\right)\times\theta'_s(x,y,t) \tag{B4}$$

The latter expression may explain a relationship between a surface tracer such as temperature and SSH (Jones et al., 1998; Hausmann & Czaja, 2012), between pressure and SSH with another double vertical integration of (B3):

$$\psi'(x,y,z,t) \sim \frac{\int_{-H}^{z}N^2dz\int_{-H}^{z}\alpha_{q,\theta_s}dz'}{\int_{-H}^{0}N^2dz\int_{-H}^{z}\alpha_{q,\theta_s}dz'}g\mathrm{SSH}/f_0 \tag{B5}$$

or between PV and SSH if (B1) is used once more. Similar derivations may follow from an assumption of separability of horizontal and vertical dependences of the density field, and, the use of the hydrostatic assumption.

Statistics. Dynamics should guide or justify statistical relationships ideally. Note, however, that one may always attempt to statistically relate any variables regardless of dynamical constraints or their units. This may be at the risk of finding a loose relationship though. The following relationships between SSH and pressure/PV were sought here:

$$p'(x,y,z,t)=\alpha_{p,\mathrm{SSH}}(x,y,z)\mathrm{SSH}'(\mathrm{x,y,t}) \tag{B6}$$

$$q'(x,y,z,t)=\alpha_{q,\mathrm{SSH}}(x,y,z)\mathrm{SSH}'(\mathrm{x,y,t}) \tag{B7}$$

Given their different spectral distributions, such linear relationships cannot lead to a faithful estimation of PV across the entire wave number space as was found in the present analysis. The preceding dynamical considerations may justify however such relationships for long wavelengths.

Dynamics may be also invoked to relate parameters estimated statistically. For example, assuming PV is dominated by its stretching term and thus using (B3), the linear relationship between pressure and SSH (B6) leads to the following PV:

$$q'(x,y,z,t) \sim \partial_z\left(\frac{f_0}{N^2}\partial_z\alpha_{p,\mathrm{SSH}}(x,y,z)\right)\times\mathrm{SSH}'(x,y,t) \tag{B8}$$

Along with (B7), we then expect the following verifiable relationship:

$$\alpha_{q,\mathrm{SSH}}(x,y,z) \sim \partial_z\left(\frac{f_0}{N^2}\partial_z\alpha_{p,\mathrm{SSH}}(x,y,z)\right) \tag{B9}$$

Acknowledgments
The authors deeply thank reviewers for their review. We gratefully acknowledge Jean-Marc Molines, Aurélie Albert, and Claude Talandier for providing the simulation data and offering the technical support. We also are thankful to Guillaume Maze for helpful discussion and reviewers for helpful comments. Due to its large size (20TB), authors had no means to deposit the NATL60 data set on an online repository. Please contact Julien Le Sommer (julien.lesommer@univ-grenoble-alpes.fr) in order to determine alternative means to access the data. The analysis of the numerical simulation was achieved with xarray/dask libraries (Dask Development Team, 2016; Hoyer, 2017). The code performing PV inversions is accessible at https://github.com/apatlpo/qgsolver. A. Ponte work was partly supported by the "Laboratoire d'Excellence" LabexMER (ANR-10-LABX-19). This work was carried out as part of the Copernicus Marine Environment Monitoring Service (CMEMS) DIMUP project. CMEMS is implemented by Mercator Ocean in the framework of a delegation agreement with the European Union.

References

Assassi, C., Y., Morel, F., Vandermeirsch, A., Chaigneau, C., Pegliasco, R., Morrow, F., et al. (2016). An index to distinguish surface-and subsurface-intensified vortices from surface observations. *Journal of Physical Oceanography*, *46*(8), 2529–2552.

Barnier, B., Madec, G., Penduff, T., Molines, J.-M., Treguier, A.-M., Sommer, J., et al. (2006). Impact of partial steps and momentum advection schemes in a global ocean circulation model at eddy-permitting resolution. *Ocean Dynamics*, *56*(5–6), 543–567.

Bretherton, F. P. (1966). Critical layer instability in baroclinic flows. *Quarterly Journal of the Royal Meteorological Society*, *92*, 325–334.
Chelton, D. B., & Wentz, F. J. (2005). Global microwave satellite observations of sea surface temperature for numerical weather prediction and climate research. *Bulletin of the American Meteorological Society*, *86*(8), 1097–1115.
Dai, A., & Trenberth, K. E. (2002). Estimates of freshwater discharge from continents: Latitudinal and seasonal variations. *Journal of Hydrometeorology*, *3*(6), 660–687.
Dask Development Team (2016). *Dask: Library for dynamic task scheduling*. Retrieved from http://dask.pydata.org
Ducet, N., Traon, P. Y. L., & Reverdin, G. (2000). Global high-resolution mapping of ocean circulation from TOPEX/Poseidon and ERS-1 and −2. *Journal of Geophysical Research*, *105*(C8), 19477–19498.
Ducousso, N., Le Sommer, J., Molines, J.-M., & Bell, M. (2017). Impact of the symmetric instability of the computational kind on oceanic hindcasts at mesoscale and submesoscale permitting resolutions. *Ocean Modelling*, *120*, 18–26.
Dussin, R., Barnier, B., & Brodeau, L. (2014). *The making of DRAKKAR forcing set DFS5* (DRAKKAR/MyOcean Rep. 05–10-14). Grenoble, France: LGGE.
Edwards, C. A., Moore, A. M., Hoteit, I., & Cornuelle, B. D. (2015). Regional ocean data assimilation. *Annual Review of Marine Science*, *7*, 21–42.
Ferry, N., Parent, L., Garric, G., Bricaud, C., Testut, C., Le Galloudec, O., et al. (2012). GLORYS2v1 global ocean reanalysis of the altimetric era (1992–2009) at meso scale. *Mercator Ocean–Quarterly Newsletter*, *44*, 29–39.
Feucher, C., Maze, G., & Mercier, H. (2016). Mean structure of the North Atlantic subtropical permanent pycnocline from in situ observations. *Journal of Atmospheric and Oceanic Technology*, *33*(6), 1285–1308.
Fu, L.-L., Alsdorf, D., Morrow, R., Rodriguez, E., & Mognard, N. (Eds.). (2012). *SWOT: The surface water and ocean topography mission*. Pasadena, CA: Jet Propulsion Laboratory.
Gaspar, P., Grégoris, Y., & Lefevre, J.-M. (1990). A simple eddy kinetic energy model for simulations of the oceanic vertical mixing: Tests at station Papa and long-term upper ocean study site. *Journal of Geophysical Research*, *95*(C9), 16179–16193.
Guinehut, S., Dhomps, A., Larnicol, G., & Le Traon, P.-Y. (2012). High resolution 3D temperature and salinity fields derived from in situ and satellite observations. *Ocean Science*, *8*(5), 845–857.
Guinehut, S., Le Traon, P.-Y., & Larnicol, G. (2006). What can we learn from Global Altimetry/Hydrography comparisons? *Geophysical Research Letters*, *33*, L10604. https://doi.org/10.1029/2005GL025551
Hausmann, U., & Czaja, A. (2012). The observed signature of mesoscale eddies in sea surface temperature and the associated heat transport. *Deep Sea Research Part I: Oceanographic Research Papers*, *70*, 60–72.
Hoyer, S., & Hamman, J. (2017). xarray: N-D labeled arrays and datasets in Python. *Journal of Open Research Software*, *5*(1). https://doi.org/10.5334/jors.148
Isern-Fontanet, J., Chapron, B., Lapeyre, G., & Klein, P. (2006). Potential use of microwave sea surface temperatures for the estimation of ocean currents. *Geophysical Research Letters*, *33*, L24608. https://doi.org/10.1029/2006GL027801
Isern-Fontanet, J., Lapeyre, G., Klein, P., Chapron, B., & Hecht, M. W. (2008). Three-dimensional reconstruction of oceanic mesoscale currents from surface information. *Journal of Geophysical Research*, *113*, C09005. https://doi.org/10.1029/2007JC004692
Jones, M. S., Allen, M., Guymer, T., & Saunders, M. (1998). Correlations between altimetric sea surface height and radiometric sea surface temperature in the South Atlantic. *Journal of Geophysical Research*, *103*(C4), 8073–8087.
Kang, D., & Curchitser, E. N. (2013). Gulf Stream eddy characteristics in a high-resolution ocean model. *Journal of Geophysical Research: Oceans*, *118*, 4474–4487. https://doi.org/10.1002/jgrc.20318
Kang, D., & Curchitser, E. N. (2015). Energetics of eddy–mean flow interactions in the Gulf Stream region. *Journal of Physical Oceanography*, *45*(4), 1103–1120.
Klein, P., Isern-Fontanet, J., Lapeyre, G., Roullet, G., Danioux, E., Chapron, B., et al. (2009). Diagnosis of vertical velocities in the upper ocean from high resolution sea surface height. *Geophysical Research Letters*, *36*, L12603. https://doi.org/10.1029/2009GL038359
LaCasce, J. H., & Mahadevan, A. (2006). Estimating subsurface horizontal and vertical velocities from sea-surface temperature. *Journal of Marine Research*, *64*, 695–721.
Lapeyre, G. (2009). What vertical mode does the altimeter reflect? On the decomposition in baroclinic modes and on a surface-trapped mode. *Journal of Physical Oceanography*, *39*, 2857–2874.
Lapeyre, G. (2017). Surface quasi-geostrophy. *Fluids*, *2*(1), 7.
Lapeyre, G., & Klein, P. (2006). Dynamics of the upper oceanic layers in terms of surface quasigeostrophy theory. *Journal of Physical Oceanography*, *36*, 165–176.
Le Sommer, J., Penduff, T., Theetten, S., Madec, G., & Barnier, B. (2009). How momentum advection schemes influence current-topography interactions at eddy permitting resolution. *Ocean Modelling*, *29*(1), 1–14.
Le Traon, P. Y. (2013). From satellite altimetry to Argo and operational oceanography: Three revolutions in oceanography. *Ocean Science*, *9*, 901–915. https://doi.org/10.5194/os-9-901-2013
Lindstrom, S. S., Qian, X., & Watts, D. R. (1997). Vertical motion in the Gulf Stream and its relation to meanders. *Journal of Geophysical Research*, *102*(C4), 8485–8503.
Madec, G., & Imbard, M. (1996). A global ocean mesh to overcome the North Pole singularity. *Climate Dynamics*, *12*(6), 381–388.
Madec, G., & The NEMO Team. (2008). NEMO ocean engine, *Note du Pôle de modélisation, Institut Pierre-Simon Laplace (IPSL), France*, *27*, 1288–1619. Retrieved from https://www.nemo-ocean.eu/doc
Meinen, C. S., & Luther, D. S. (2016). Structure, transport, and vertical coherence of the Gulf Stream from the Straits of Florida to the southeast newfoundland ridge. *Deep Sea Research Part I: Oceanographic Research Papers*, *112*, 137–154.
Mellor, G. L., & Ezer, T. (1995). Sea level variations induced by heating and cooling: An evaluation of the Boussinesq approximation in ocean models. *Journal of Geophysical Research*, *100*(C10), 20565–20577.
Mulet, S., Rio, M.-H., Mignot, A., Guinehut, S., & Morrow, R. (2012). A new estimate of the global 3D geostrophic ocean circulation based on satellite data and in-situ measurements. *Deep Sea Research Part II: Topical Studies in Oceanography*, *77*, 70–81.
Olson, D. B. (1991). Rings in the ocean. *Annual Review of Earth and Planetary Sciences*, *19*(1), 283–311.
Ponte, A. L., & Klein, P. (2013). Reconstruction of the upper ocean 3D dynamics from high resolution sea surface height. *Ocean Dynamics*, *63*(7), 777–791. https://doi.org/10.1007/s10236-013-0611-7
Reul, N., Chapron, B., Lee, T., Donlon, C., Boutin, J., & Alory, G. (2014). Sea surface salinity structure of the meandering Gulf Stream revealed by SMOS sensor. *Geophysical Research Letters*, *41*, 3141–3148. https://doi.org/10.1002/2014GL059215
Rio, M.-H., & Hernandez, F. (2004). A mean dynamic topography computed over the world ocean from altimetry, in situ measurements, and a geoid model. *Journal of Geophysical Research*, *109*, C12032. https://doi.org/10.1029/2003JC002226
Rio, M.-H., Santoleri, R., Bourdalle-Badie, R., Griffa, A., Piterbarg, L., & Taburet, G. (2016). Improving the altimeter-derived surface currents using high-resolution sea surface temperature data: A feasability study based on model outputs. *Journal of Atmospheric and Oceanic Technology*, *33*(12), 2769–2784.

Rossby, T., Flagg, C., & Donohue, K. (2010). On the variability of Gulf Stream transport from seasonal to decadal timescales. *Journal of Marine Research*, *68*(3-1), 503–522.
Sanchez de La Lama, M., LaCasce, J., & Fuhr, H. K. (2016). The vertical structure of ocean eddies. *Dynamics and Statistics of the Climate System*, *1*(1), dzw001.
Savidge, D. K. (2016). Comment on: Structure, transport, and vertical coherence of the Gulf Stream from the Straits of Florida to the southeast Newfoundland Ridge, by Meinen and Luther. *Deep Sea Research Part I: Oceanographic Research Papers*, *112*, 155–157.
Savidge, D. K., & Bane, J. M. (1999). Cyclogenesis in the deep ocean beneath the Gulf Stream: 1. Description. *Journal of Geophysical Research*, *104*(C8), 18111–18126.
Shay, T. J., Bane, J. M., Watts, D. R., & Tracey, K. L. (1995). Gulf Stream flow field and events near 68 W. *Journal of Geophysical Research*, *100*(C11), 22565–22589.
Smith, K. S., & Vallis, G. K. (2001). The scales and equilibration of midocean eddies: Freely evolving flow. *Journal of Physical Oceanography*, *31*, 554–571.
Stammer, D. (1997). Global characteristics of ocean variability estimated from regional TOPEX/Poseidon altimeter measurements. *Journal of Physical Oceanography*, *27*(8), 1743–1769.
Sutyrin, G. (2015). Why compensated cold-core rings look stable. *Geophysical Research Letters*, *42*, 5395–5402. https://doi.org/10.1002/2015GL064378
The Ring Group. (1981). Gulf Stream cold-core rings: Their physics, chemistry, and biology. *Science*, *212*, 1091–1100.
Ubelmann, C., Cornuelle, B., & Fu, L. (2016). Dynamic mapping of along-track ocean altimetry: Method and performance from observing system simulation experiments. *Journal of Physical Oceanography*, *33*, 1691–1699.
Ubelmann, C., Klein, P., & Fu, L.-L. (2015). Dynamic interpolation of sea surface height and potential applications for future high-resolution altimetry mapping. *Journal of Atmospheric and Oceanic Technology*, *32*, 177–184.
Wang, J., Flierl, G. R., LaCasce, J. H., McClean, J. L., & Mahadevan, A. (2013). Reconstructing the ocean's interior from surface data. *Journal of Physical Oceanography*, *43*, 1611–1626.
Watts, D. R., Tracey, K. L., Bane, J. M., & Shay, T. J. (1995). Gulf Stream path and thermocline structure near 74 W and 68 W. *Journal of Geophysical Research*, *100*(C9), 18291–18312.
Willis, J. K., & Fu, L. (2008). Combining altimeter and subsurface float data to estimate the time-averaged circulation in the upper ocean. *Journal of Geophysical Research*, *113*, C12017. https://doi.org/10.1029/2007JC004690
Wunsch, C. (1997). The vertical partition of oceanic horizontal kinetic energy. *Journal of Physical Oceanography*, *27*(8), 1770–1794.
Wunsch, C. (2015). *Modern observational physical oceanography: Understanding the global ocean*. Princeton, NJ: Princeton University Press.